12. B. van der Pol and J. van der Mark, *Philos. Mag.* **6**, 763 (1928); S. D. Moulopoulos, N. Kardaras, D. A. Sideris, *Am. J. Physiol.* **208**, 154 (1965); J. V. O. Reid, *Am. Heart J.* **78**, 58 (1969); F. A. Roberge and R. A. Nadeau, *Can. J. Physiol. Pharmacol.* **42**, 695 (1969); D. A. Sideris and S. D. Moulopous, *J. Electrocardiol.* **10**, 51 (1977); C. R. Katholi, F. Urthaler, J. Macy, T. N. James, *Comp. Biomed. Res.* **10**, 529 (1977).
13. R. Langendorff, *Am. Heart J.* **55**, 181 (1958).
14. Supported by grants from the Canadian Heart Foundation and the Natural Sciences and Engineering Research Council of Canada. M.R.G. is a recipient of a predoctoral traineeship from the Canadian Heart Foundation. We thank D. Colizza for technical assistance and M. C. Mackey and A. T. Winfree for helpful conversations.

3 August 1981; revised 13 October 1981

Computer Averaging of Electron Micrographs of 40*S* Ribosomal Subunits

Abstract. *An enhanced lateral view of the 40S ribosomal subunit of HeLa cells has been obtained by computer averaging of single particles visualized in the electron microscope. Application of crystallographic criteria to independent averages shows that the reproducibility of the result is comparable to that obtained for thin, stained protein crystals by conventional Fourier filtration methods.*

Ribosomes are ribonucleoprotein particles that process the genetic information coded in messenger RNA (mRNA) for protein synthesis (*1*). Knowledge of their conformation is important for understanding their function in the assembly of polypeptide chains. Visualization by high-resolution electron microscopy offers obvious advantages for the study of the morphology of ribosomes. However, the large amount of noise in electron micrographs precludes detailed analysis, unless some method of image averaging (*2*, *3*) is employed. Studies of crystalline ribosome aggregates (*4*) have failed to give high-resolution structural information, because of the residual disorder in the arrangement of the ribosomes. We have used the computer to align and average large numbers of individual images corresponding to a single view of the ribosomal particle (*3*) for structural analysis of the small (40*S*) ribosomal subunit from HeLa cells [preliminary account in (*5*)].

Specimens for conventional transmission electron microscopy were prepared (*6*). A 0.5 percent aqueous uranyl acetate solution (not adjusted for *p*H) was used as contrasting stain. The grids were examined in an electron microscope (JEM 100B) operated at 80 kV, with a magnification of 70,000. The subunits (Fig. la) appear as elongate particles, approximately 250 by 130 Å, and display a strong preference for orientations referred to as right (R) and left (L) lateral views (*7*). The most characteristic structural feature is a beaklike protrusion (Fig. la, arrow).

Small areas containing particles in the L lateral view were selected from several electron micrographs and scanned into 128 by 128 arrays at 7.14 Å resolution. Each array was displayed on a computer-linked halftone monitor for interactive selection of a 64 by 64 window containing the particle (*8*).

A mask with a radius of 25 units (corresponding to 178 Å) was applied to each image to reduce the influence of noise in the further processing. Seventy-seven such masked arrays were aligned (Fig. 1b) by using auto- and cross-correlation functions (*3*, *9*), with one particle selected as reference. The reference particle was low-pass filtered (see Fig. 2b, legend) to a resolution of 1/28 $Å^{-1}$ to eliminate high-resolution portions of the noise. After the first alignment pass, the alignment was refined in two cycles, with the average of the previous cycle used as reference each time.

The first pass aligned the particles to within a few degrees of the reference. This approximate positioning allowed use of the direct method of orientation search (*10*) in the subsequent refinement cycles, in which the image, rather than its autocorrelation function, was subjected to the rotational cross-correlation. The combination of autocorrelation (*9*) and direct (*10*) methods was found to give a higher reproducible resolution in the final average than was given by the autocorrelation method alone.

The average of 77 aligned images (Fig. 2, a and b) shows the 40*S* subunit to have a complex morphology. It appears to be divided by stain incursions into three major regions, each characterized by three prominent minima in stain density.

Several different methods were used to ascertain the validity of the result: comparison of independent averages, analysis of the variance associated with

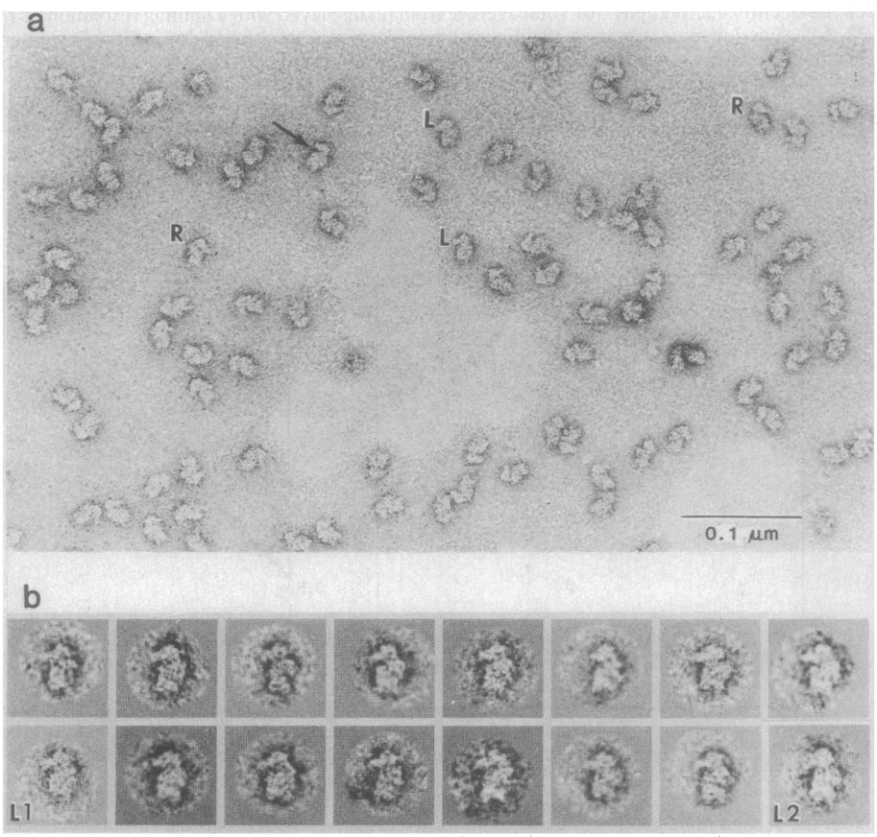

Fig. 1. (a) Electron micrograph showing left-oriented (L) and right-oriented (R) lateral views of 40*S* ribosomal subunits of HeLa cells. The particles in L views were selected for processing. Arrow points to the characteristic beaklike protrusion. (b) Gallery showing 16 of the 77 particles after alignment. L1 and L2 were used as the initial reference particles in the alignments.

0036-8075/81/1218-1353$01.00/0

the averaging of each image point, and quantitative comparison of the Fourier transforms of the averages. We concluded that the observed stain density minima are significant, and their locations vary by less than 6 Å. The overall reproducibility of the averaged projection of subunit and surrounding stain was found to be 1/32 $Å^{-1}$.

The images were arbitrarily split into two sets of 38 and 39, which were averaged separately (Fig. 2, c and d). The independent averages agree with one another and with the total average (Fig. 2a) in all major features. The positions of each of the nine density minima differ by not more than 6 Å. The difference image (Fig. 2e) reveals that the main density differences are in regions where the stain penetrates the particle.

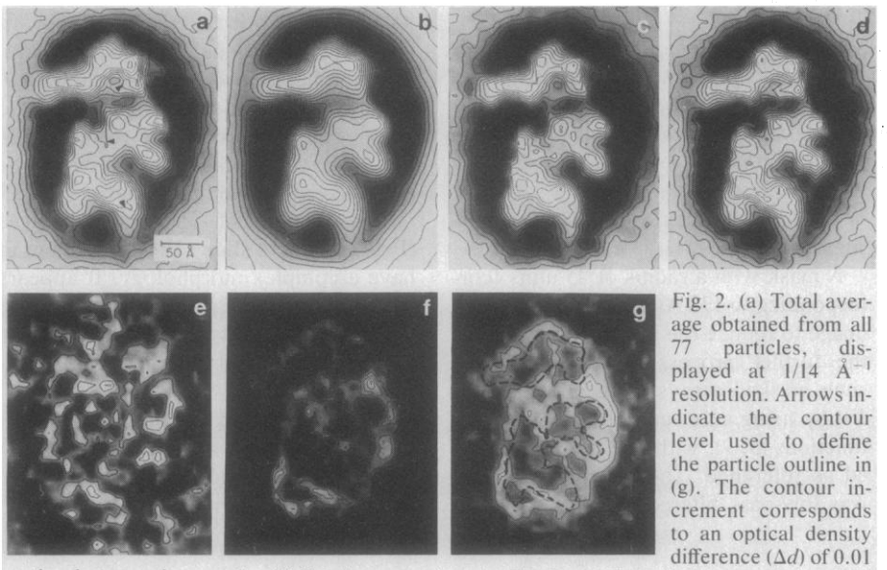

Fig. 2. (a) Total average obtained from all 77 particles, displayed at 1/14 $Å^{-1}$ resolution. Arrows indicate the contour level used to define the particle outline in (g). The contour increment corresponds to an optical density difference (Δd) of 0.01 on the electron micrographs. (b) Total average from (a) displayed with a limiting resolution of 1/32 $Å^{-1}$. For low-pass filtration the Fourier transform was multiplied by a Gaussian filter function that falls to 1/*e* at the limiting resolution. The contouring increment is $\Delta d = 0.0075$. (c and d) Averages obtained from independent sets of 38 and 39 particles, displayed at 1/14 $Å^{-1}$ resolution. The initial reference particle was L1 (Fig. 1b). The contour increment was the same as in (a). (e) Difference image of the averages in (c) and (d), displayed with the same contour increment. (f) Display of variance for total average image in (a), contoured with a 0.005 increment. (g) Display of standard deviation for (a), contoured with $\Delta d = 0.01$. The dashed line delimits the particle outline as defined by a selected contour level in (a).

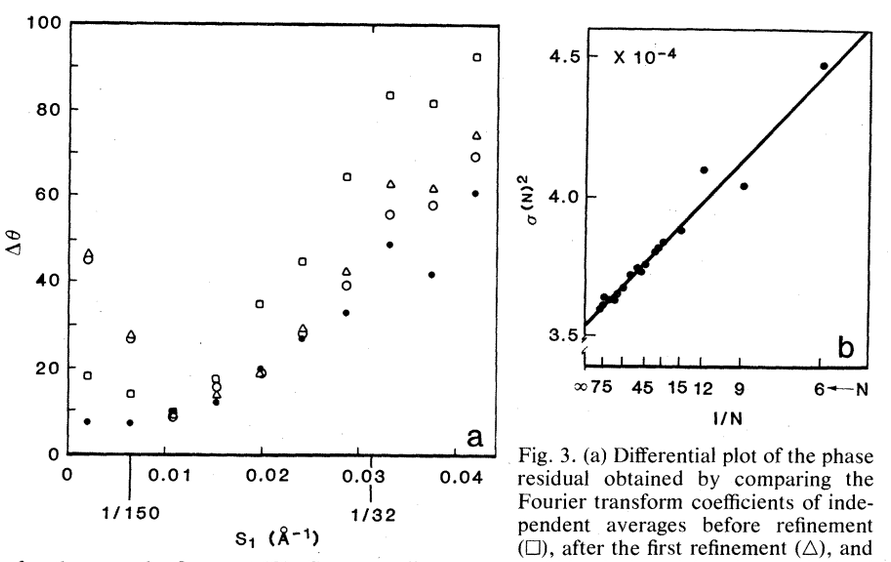

Fig. 3. (a) Differential plot of the phase residual obtained by comparing the Fourier transform coefficients of independent averages before refinement (□), after the first refinement (△), and after the second refinement (○). Corresponding averages of identical particle subsets, obtained with different initial reference particles (L1 and L2 in Fig. 1b), were also compared (●). Summation according to Eq. 3 in Fourier space is carried out over concentric ring zones $s = s_1 \pm \Delta s$ with $\Delta s = 0.0022$ $Å^{-1}$, and the results are plotted as a function of s_1. (b) Variance of the average image as a function of 1/*N*, where *N* is the number of particles averaged. The plot shows the expected linear behavior for large *N* and enables the gain in s/n to be determined.

To test the significance of features observed in the average, we computed the variance of *N* realizations of each image element, where *N* is the number of images, according to (*11*)

$$v_{ik} = \frac{1}{N-1} \sum_{n=1}^{N} [d_{ik}^{(n)}]^2 - \bar{d}_{ik}^2 N \quad (1)$$

Here $d_{ik}^{(n)} = D_{ik}^{(n)} - \bar{D}^{(n)}$ is an array representing the *n*th image on a sampling grid indexed by (*i,k*) obtained from the original optical density measurements $D_{ik}^{(n)}$ by floating; that is, by subtracting

$$\bar{D}^{(n)} = \frac{1}{M} \sum_{i,k} D_{ik}^{(n)}$$

(where *M* is the total number of image points). In Eq. 1, the average image obtained by averaging *N* particles is denoted by

$$\bar{d}_{ik} = \frac{1}{N} \sum_{n=1}^{N} d_{ik}^{(n)} \quad (2)$$

The resulting variance image (*11*) shows high values in those areas of the image field where the images differ most (Fig. 2f). A standard deviation image (Fig. 2g) was obtained by taking the square root, point by point, of the variance image. At the resolution of scanning representation (1/14 $Å^{-1}$), the standard deviation is high (up to three contour levels) only along the borders of the stain-excluding regions (enclosed by dashed lines in Fig. 2g). Within these regions, the standard deviation of the average does not exceed one contour interval, whereas the nine strong stain density minima stand out by two or three contour intervals from the local background.

For a quantitative assessment of overall reproducibility [see (*12*)], the phase residual [for example (*13*)] was computed from the Fourier transforms F_1 and F_2 of the independent averages (Fig. 2, c and d). The phase residual is defined as

$$\Delta\theta = \left\{ \frac{\Sigma(|F_1| + |F_2|)\,(\delta\theta^2)}{\Sigma(|F_1| + |F_2|)} \right\}^{1/2} \quad (3)$$

where $\delta\theta$ is the phase difference between F_1 and F_2, and the summations extend over a certain domain of the reciprocal space. Use of this criterion is possible because the averages to be compared are aligned with respect to one another, assuring the same phase origin for the corresponding transforms.

We computed the phase residuals for annuli of equal width in reciprocal space and plotted their values as a function of radius (Fig. 3a). We found such a differ-

ential plot was best suited for determining the resolution limit of agreement in reciprocal space and for assessing the relative merits of different alignment strategies. Above 1/150 $Å^{-1}$, the phase residual decreases substantially in the refinement cycles, whereas it shows the opposite behavior at and below 1/150 $Å^{-1}$. This behavior indicates that in going from the first to the second alignment cycle, accuracy in the alignment of strongly variable, low-resolution features of the outer stain layer is traded off for an increased accuracy in the alignment of high-resolution features.

By allowing a maximum phase residual of 45°, we obtain from Fig. 3a a limiting resolution of 1/32 $Å^{-1}$. Indeed, the total average of Fig. 2a when limited to this resolution (Fig. 2b) still shows the prominent features observed in the unfiltered average.

The phase residual was also used to check the dependence of the result on the choice of the initial reference. We repeated the entire three-cycle alignment procedure with a different particle as reference and determined the phase residual of averages over the same particle subset (Fig. 2c) obtained with the two different reference particles. The values of the phase residual (Fig. 3a) indicate that the agreement is closer than the agreement between averages over different subsets obtained with the same reference particle. This result is to be expected for the limited number of particles used.

A plot of the variance as a function of the number of images N averaged allows the gain in signal-to-noise ratio (s/n) to be determined (*14*). The variance of the average image, $\sigma^{(N)^2}$, is expected to decrease according to

$$\sigma^{(N)^2} = \sigma^2 + \frac{1}{N}\sigma_n^2 \qquad (4)$$

where σ^2 is the variance of the signal common to the image set and σ_n^2 the variance of the noise, modeled as Gaussian and additive. Plotting $\sigma^{(N)^2}$ as a function of $1/N$ shows an approximately linear dependence above $N = 6$ (Fig. 3b). From the slope and intersection of the straight line with the variance axis ($N = \infty$), we could calculate the average initial s/n, $\sigma^2/\sigma_n^2 = 0.55$, and the residual s/n in the average of all particles (Fig. 2a), $(N\sigma^2)/\sigma_n^2 = 42.4$.

The reproducibility of the density distribution obtained by single-particle averaging approaches that of maps obtained by Fourier averaging of micrographs of ordered protein arrays [see, for example (*15*)]. In this range of accuracy, rounding errors and errors of interpolation in the digital analysis must be seriously considered.

The approach of single-particle averaging rests on the assumption that all of the images are comparable. However, interparticle variations, which will tend to blur the averaged image, arise from several sources. The strength of the outer stain layer varies relative to the mean density of the stain-excluding regions. The effective tilt angle may also vary. The lateral view analyzed may, in fact, comprise a small range of tilted views of the 40*S* subunit, with the tilt axis likely parallel to the particle's long axis.

Greater homogeneity of the image set to be averaged—and thus finer resolvable detail—can be obtained through application of multivariate statistical analysis (*16*). Even without this refinement, the realization of a quantitatively reproducible, averaged projection is a major step toward a high-resolution, three-dimensional model of the ribosome structure.

JOACHIM FRANK
ADRIANA VERSCHOOR
Division of Laboratories and Research, New York State Department of Health, Albany 12201

MILOSLAV BOUBLIK
Roche Institute of Molecular Biology, Nutley, New Jersey 07110

References and Notes

1. G. Chambliss, G. R. Craven, J. Davies, K. Davis, L. Kahan, M. Nomura, Eds., *Ribosomes* (University Park Press, Baltimore, 1980).
2. R. Markham, D. Hitchborn, G. Hills, S. Frey, *Virology* **22**, 342 (1964); F. P. Ottensmeyer, J. W. Andrew, D. P. Bazett-Jones, A. S. K. Chan, J. Hewitt, *J. Microsc.* **109**, 259 (1977); A. Klug and D. J. DeRosier, *Nature (London)* **212**, 29 (1966); H. P. Erickson and A. Klug, *Ber. Bunsenges. Phys. Chem.* **74**, 1129 (1970); G. Lutsch, K.-P. Pleissner, G. Wangermann, F. Noll, *Acta Biol. Med. Germ.* **36**, K-59 (1977).
3. J. Frank, W. Goldfarb, D. Eisenberg, T. S. Baker, *Ultramicroscopy* **3**, 283 (1978).
4. P. N. T. Unwin and C. Taddei, *J. Mol. Biol.* **114**, 491 (1977); W. Kühlbrandt and P. N. T. Unwin, in *Electron Microscopy at Molecular Dimensions*, W. Baumeister and W. Vogell, Eds. (Springer-Verlag, Berlin, 1980), pp. 108–116.
5. M. Boublik, J. Frank, B. Tesche, A. Verschoor, *Proc. Electron Microsc. Soc. Am.* **39**, 43 (1981).
6. M. Boublik, W. Hellmann, A. K. Kleinschmidt, *Cytobiologie* **14**, 293 (1977).
7. M. Boublik and W. Hellmann, *Proc. Natl. Acad. Sci. U.S.A.* **75**, 2829 (1978).
8. J. Frank, *Proc. 9th Int. Congr. Electron Microsc.* **3**, 87 (1978); ——— and B. Shimkin, *ibid.* **1**, 210 (1978); ———, H. Dowse, *Ultramicroscopy* **6**, 343 (1981).
9. J. Frank, *Ultramicroscopy* **1**, 159 (1975).
10. M. Steinkilberg and H. J. Schramm, *Hoppe-Seyler's Z. Physiol. Chem.* **361**, 1363 (1980).
11. J. L. Carrascosa and A. Steven, *Micron* **9**, 199 (1978).
12. J. Frank, *J. Microsc.* **117**, 25 (1979).
13. P. N. T. Unwin and A. Klug, *J. Mol. Biol.* **87**, 641 (1974).
14. W. Haenicke and H. P. Zingsheim have used this plot in a study of the reproducibility of acetylcholine receptor averages obtained by the same method of averaging.
15. T. S. Baker and L. A. Amos, *J. Mol. Biol.* **123**, 89 (1978).
16. M. van Heel and J. Frank, *Ultramicroscopy* **6**, 187 (1981).
17. We thank P. N. T. Unwin for a critical reading of the manuscript and D. DeRosier for discussions.

1 June 1981; revised 23 September 1981

Regulation of Muscle Differentiation: Stimulation of Myoblast Fusion in vitro by Catecholamines

Abstract. *Epinephrine and isoproterenol provoke primary chick myoblasts to initiate precocious cell fusion. Both the rise in intracellular adenosine 3',5'-monophosphate (cyclic AMP) and cell fusion generated by these effectors are prevented by propranolol, which is a specific blocker of the β-adrenergic receptor. Propanolol has no effect either on the precocious cell fusion provoked by prostaglandin E or on cell fusion in control cultures. The results support the idea that a rise in cyclic AMP is the critical intracellular change responsible for initiating events that culminate in myoblast differentiation 4 to 5 hours later. They also indicate that the hormone responsible for the positive regulation of myoblast differentiation in vitro is not acting through the β-adrenergic receptor.*

Myoblast differentiation involves the fusion of cell membranes to form the postmitotic multinucleate units characteristic of adult skeletal muscle tissue and the concomitant elaboration of muscle-specific proteins such as the acetylcholine (ACh) receptor, the contractile proteins, and the muscle-specific form of creatine phosphokinase. The initial stages of muscle differentiation do not depend on changes that result from cell fusion (*1–4*). Nevertheless, the temporal correlation between the appearance of some muscle-specific products and myoblast fusion (*5*) suggests the existence of a coordinating regulatory mechanism. A central question related to muscle differentiation is therefore the nature of the control mechanisms that regulate the transition from the proliferating single cell to the differentiated postmitotic multinucleate unit and that coordinate the appearance of the different aspects of the cells' differentiated state.

Several lines of evidence suggest that cyclic nucleotides play an important role in the regulation of muscle differentiation. First, a transient rise in intracellular adenosine 3',5'-monophosphate (cyclic AMP) occurs shortly before the onset of

0036-8075/81/1218-1355$01.00/0